ACS APPLIED MATERIALS & INTERFACES

Research Article

www.acsami.org

Up-Conversion Nanoparticle Assembled Mesoporous Silica Composites: Synthesis, Plasmon-Enhanced Luminescence, and Near-Infrared Light Triggered Drug Release

Na Niu,[†] Fei He,[†] Ping'an Ma,[‡] Shili Gai,[†] Guixin Yang,[†] Fengyu Qu,*[,§] Yan Wang,[†] Jie Xu,[†] and Piaoping Yang*[,†]

[†]Key Laboratory of Superlight Materials and Surface Technology, Ministry of Education, College of Materials Science and Chemical Engineering, Harbin Engineering University, Harbin, Heilongjiang 150001, P. R. China

[‡]State Key Laboratory of Rare Earth Resource Utilization, Changchun Institute of Applied Chemistry, Chinese Academy of Sciences, Changchun, Jilin 130022, P. R. China

[§]Key Laboratory of Semiconductor Nanocomposite Materials, Ministry of Education, Harbin Normal University, Harbin, Heilongjiang 150025, P. R. China

Supporting Information

ABSTRACT: A facile process for the preparation of multifunctional nanospheres combining several advantages of mesoporous channels, up-conversion (UC) luminescence, and photothermal responses into one single entity is reported. First, Gd_2O_3:Yb/Er assembled mesoporous silica with 2D hexagonal (MCM-41) and 3D cubic (MCM-48) network have been prepared via a one-step procedure. Then, gold nanocrystals with diameter of 5 nm are integrated with the amino group functionalized nanocomposites. Upon 980 nm near infrared (NIR) laser irradiation, a wavelength-dependent enhancement of the UC intensities is observed due to the surface plasmon resonance (SPR) effect of attached gold nanoparticles. These composites have good biocompatibility and sustained anticancer drug (doxorubicin, DOX) release properties, making it a promising candidate for drug delivery. Particularly, under 980 nm NIR laser irradiation, the green UC emission overlaps the SPR band of gold nanocrystals, which causes a photothermal effect of gold nanocrystals and induces a rapid DOX release from the Au hybrid materials. This DOX loaded multifunctional system has an obvious cytotoxic effect and photothermally killing enhanced effect on SKOV3 ovarian cancer cells. The endocytosis process was also demonstrated through confocal laser scanning microscope (CLSM) images. Such novel multifunctional anticancer drug delivery systems, which combine hyperthermia with the chemotherapeutic drugs by synergistic effect, should be of high potential in cancer therapy.

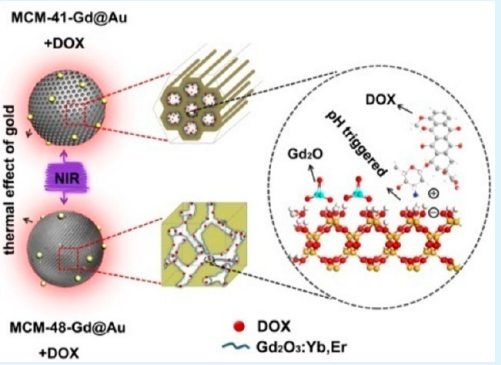

KEYWORDS: *mesoporous silica, up-conversion, plasmon-enhancement, drug release*

INTRODUCTION

During the past decade, rapid progress has been made on the design and exploitation of nanoparticles as carriers for an anticancer drug delivery system.[1−4] An inorganic nanoparticle-based drug delivery system is one important branch and has received considerable attention based on its unique advantages in several aspects, such as being easy to prepare and having fine control of the size and morphology, a large surface area and volume for drug loading, and a high stability in a physiological environment.[5,6] Until now, diverse inorganic systems have been developed as anticancer drug delivery systems, including iron oxides,[7] carbon nanohorns and nanotubes,[8,9] $NaREF_4$ up-conversion (UC) nanoparticles,[10−13] hollow gold nanoparticles,[14] mesoporous silica-based materials,[15−22] etc. Among them, mesoporous silica-based particles have obtained the most attention for biological applications due to their excellent biocompatibility, in vivo biodegradability, and the capability to be functionalized with different organic groups. Especially, the 2D ordered hexagonal MCM-41[23−25] and 3D ordered cubic MCM-48[20] molecular sieve with large BET surface area (>1000 m^2/g), tunable pore volume, and uniform porosity are attractive candidates as drug carriers.

Lanthanide doped UC luminescent materials can convert low-energy photons into high-energy photons based the anti-Stokes process, which have been used for biological labeling, imaging, therapy, sensing, etc.[26−33] This kind of material possesses advantages of sharp absorption and emission lines, deep tissue penetration, weak autofluorescence, and high signal-

Received: November 11, 2013
Accepted: February 12, 2014
Published: February 12, 2014

Scheme 1. Diagram Showing the Structure of DOX Loaded MCM-41-Gd@Au and MCM-48-Gd@Au

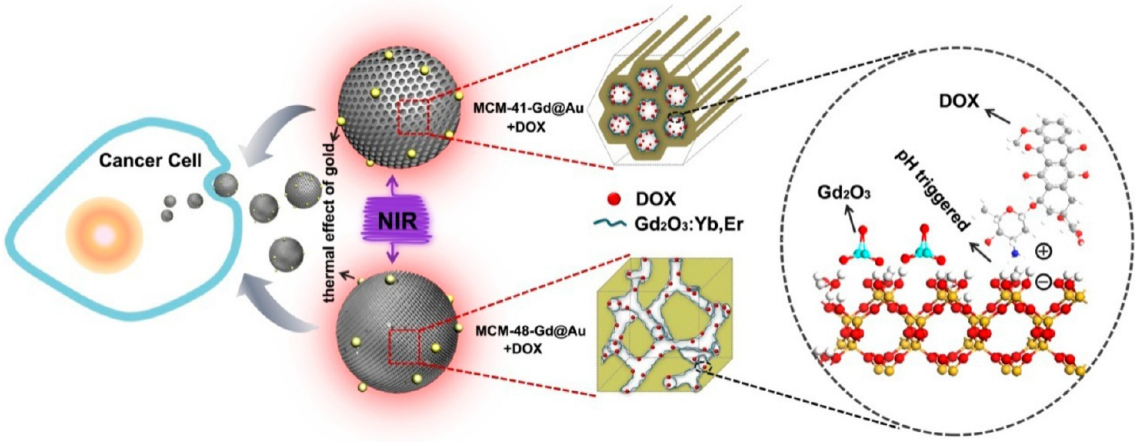

to-noise ratio.[34−42] For the purpose of using UC materials as drug carriers, the traditional way is to build a core−shell structured composite, which will always block the pore channels.[19,43] On the other hand, the involved postgrafting/deposition process to functionalize fluorescence usually leads to the dramatic decrease of the specific surface area and pore volume, which will greatly limit their application in biomedical fields.[44,45] Therefore, developing a one-step in situ route for the synthesis of bifunctional composite combining the ordered mesopores and the RE-based UC luminescence properties together should be highly promising, because the in situ one-step will not destroy the mesoporous structure, and the drug loading capacity of the nanocomposites can be highly improved.

Using the noble metal shell or nanostructures to adjust the UC luminescence through the localized surface plasmon resonance (SPR) effect has been widely reported.[46−50] The optical response, SPRs, and local field distributions are highly dependent on the particle shape, size, and distribution, the interaction between particles, and the polarization of the incident light.[51,52] On one hand, the attachment of gold nanoparticles can greatly enhance the UC emission intensities by increasing the incident electromagnetic field arising from the SPR of metal. On the other hand, some spectral fluorescence can be reduced by nanoradiative energy transfer from the phosphor to the metal via SPR absorption. In this Article, we modified the UC luminescent nanoparticle assembled ordered mesoporous silica with plasmonic gold nanocrystals attached onto their surface. The small gold nanocrystals in our experiment have a strong absorption band at around 530 nm, which overlaps the position of green emission from Gd_2O_3:Yb,Er. Therefore, the gold nanocrystal hybrid samples present a wavelength-dependent UC enhancement. Moreover, gold nanocrystals are highly efficient photothermal convertors, which offer a way to influence the drug release process.[53−56] Upon 980 nm near infrared (NIR) irradiation, the attached gold nanocrystals can absorb green output and convert the energy into heat. The heat disperses into the surroundings and causes a rise in temperature, which can increase the membrane permeability and promotes the destruction of biological samples. The light induced hyperthermia is considered as a relatively noninvasive and benign adjuvant/alternative for cancer treatment. Combined with the anticancer drugs, this system provides a high potential application in cancer therapy. A diagram showing the design of the mesopore structure as well as its doxorubicin (DOX) loading and release is exhibited in Scheme 1.

EXPERIMENTAL SECTION

Materials. $GdCl_3·6H_2O$ (99.99%), $YbCl_3·6H_2O$ (99.99%), $ErCl_3·6H_2O$ (99.99%), Pluronic F127, and $HAuCl_4$ were purchased from Sinopharm Chemical Reagent Co., Ltd. *N*-Cetytrimethylammonium bromide (CTAB, 99%), NaOH (99%), TEOS (A. R.), sodium citrate (99%), tannic acid(99%), and acetic acid were purchased from Beijing Yili Fine Chemicals Co., Ltd. DOX was purchased from the Nanjing Duodian Chemical Co., Ltd. All the reagents were used as received without further purification.

Synthesis of MCM-41-Gd and MCM-48-Gd. The Gd_2O_3:Yb^{3+},Er^{3+} assembled MCM-41 with 2D hexagonal network of pores (denoted as MCM-41-Gd) and MCM-48 with cubic network of pores (denoted as MCM-48-Gd) were synthesized through modifying the MCM-41[57] and MCM-48[58] synthesis procedure. As for MCM-41-Gd, 1.0 g of CTAB was first dissolved in 480 mL of deionized water containing 0.5 g of NaOH. After stirring at 80 °C for 1 h, 5 mL of TEOS was added dropwise into the solution within 5 min. The mixture was further stirred for 30 min before 0.89 mmol of $GdCl_3·6H_2O$, 0.1 mmol of $YbCl_3·6H_2O$, and 0.01 mmol of $ErCl_3·6H_2O$ was added. After another 1.5 h, the precipitate was filtered, washed with deionized water, and dried overnight at room temperature. For the synthesis of MCM-48-Gd, 1.0 g of CTAB and 4.0 g of Pluronic F127 were dissolved in 200 mL of deionized water containing 20 mL of NH_4OH and 85 mL of EtOH. Then, 5 mL of TEOS was added dropwise into the solution. After another stirring for 2 h, $GdCl_3·6H_2O$, $YbCl_3·6H_2O$, and $ErCl_3·6H_2O$ were added. After stirring for 20 h, the precipitate was filtered, washed with deionized water, and dried overnight. The two kinds of powders were then calcined at 550 °C for 5 h and 800 °C for 5 h (air, heating rate 1 °C/min) to gain the final products.

Synthesis of MCM-41-Gd@Au and MCM-48-Gd@Au Hybrid Nanostructures. The gold nanocrystals with a diameter of about 5 nm were prepared following the citrate reduction methods in the presence of tannic acid as reducing agent: 630 mL of 0.3 mM $HAuCl_4$ was mixed with a 150 mL solution containing 9.8 mM sodium citrate and 0.31 mM tannic acid and kept at 60 °C for 4 h. For the conjugating of gold nanocrystals, the surface of MCM-41-Gd and MCM-48-Gd were first modified with amino groups: a 0.02 mmol sample was dispersed in 10 mL of water containing 200 μL of acetic acid. Then, 20 μL of (3-trimethoxysilylpropyl-)-diethylenetriamine was added to the solution and stirred for 4 h. The amino-modified sample was collected by centrifugation, washed by deionized water twice, and redispersed in 10 mL of deionized water. Then, 20 mL of as-prepared gold suspension (0.25 mM) was swiftly added into the solution and slowly rotated for 2 h. The final product with molar ratio of MCM-41(48)-Gd/Au = 4/1 was collected and named as MCM-41-Gd@Au

and MCM-48-Gd@Au, respectively. In order to investigate how UC luminescence would be affected by various concentrations of gold nanoparticles, a series of MCM-41-Gd@Au and MCM-48-Gd@Au hybrid crystals with different MCM-41(48)-Gd/Au ratios were prepared through a similar process by changing the concentration of gold suspensions to 0.062, 0.125, and 0.375 mM.

Preparation of Drug Loading and Release Systems. The loading of DOX onto the MCM-41-Gd, MCM-41-Gd@Au, MCM-48-Gd, and MCM-41-Gd@Au samples were done by mixing DOX (0.5 mg/mL) with the as-prepared samples (2 mg/mL) in phosphate buffer solution (PBS, pH = 7.4, 5 mL) for 24 h. For the DOX loading saturation experiment, different concentrations of DOX (0.5−3 mg/mL) were mixed with the as-prepared samples in PBS overnight. Free DOX was removed by centrifugation at 10 000 rpm for 20 min. The precipitates were washed with PBS by centrifugation until the supernatant became colorless. The supernatants were collected and measured by UV−vis spectrophotometry at 480 nm to determine the amount of free DOX. The obtained products were denoted as MCM-41-Gd@Au+DOX and MCM-48-Gd@Au+DOX, respectively.

For the DOX release studies, the DOX loaded samples were dispersed in 10 mL of PBS (pH = 5.0, 7.4) kept at 37 °C with magnetic stirring. At certain time intervals, PBS solutions were collected by a magnet to test the DOX released percentage, while fresh PBS was added again for further drug release experiments. Especially, for the MCM-41-Gd@Au+DOX and MCM-48-Gd@Au+DOX samples, a near infrared (NIR) irradiation (980 nm, 0.5 W/cm^2) was used during the whole drug release process. The laser probe with a 15 mm spot diameter was placed on the top of the experimental tube.

Cytotoxicity of MCM-41-Gd@Au+DOX. The in vitro cytotoxicity was determined by MTT (3-(4,5-dimethylthiazol-2-yl)-2,5-diphenyltetrazolium bromide) assays against human SKOV3 ovarian cancer cells. Human SKOV3 ovarian cancer cells with density of 8000 cells per well were plated in a 96-well plate in 5% CO_2 at 37 °C for 24 h to allow the cells to attach. The cells were exposed to free DOX and MCM-41-Gd@Au+DOX with different concentrations. Then, the cells were incubated at 37 °C for 24 h in 5% CO_2. At the end of the incubation time, the medium was removed and MTT solution (20 μL, diluted in a culture medium to a final concentration of 0.8 mg/mL) was added. After incubation at 37 °C for 4 h, 150 μL of dimethyl sulfoxide (DMSO) was added to each well, and the absorbance was monitored with a microplate reader at a wavelength of 490 nm. Averages and standard deviations were based on four samples, and all tests were performed in triplicate. Meanwhile, cell viability of MCM-41-Gd@Au was also determined using MTT assay, which was the same as the procedure for the cytotoxicity assay for MCM-41-Gd@Au +DOX sample. The cell viability was calculated using the following equation: Cell viability (%) = $A_{test}/A_{control}$. (A_{test} is the average cell viability after adding the as-prepared structures; $A_{control}$ is the cell viability for the control experiment that did not add any particles.) For the in vitro photothermal therapy test, the cells incubated with different concentrations of MCM-41-Gd@Au and MCM-41-Gd@Au +DOX were first exposed to NIR light (980 nm, 0.5 W/cm^2) for 10 min before being incubated for an additional 24 h.

Cellular Uptake of MCM-41-Gd@Au+DOX. Cellular uptake by SKOV3 ovarian cancer cells was examined using a confocal laser scanning microscope (CLSM). The SKOV3 ovarian cancer cells were seeded in a 6-well culture plate (a clean coverslip was put in each well) and grown overnight as a monolayer. Then, they were incubated with as-prepared MCM-41-Gd@Au+DOX at 37 °C for 30 min and 3 h, respectively. After that, the cells were rinsed with PBS three times, fixed with 2.5% formaldehyde (1 mL/well) at 37 °C for 10 min, and then rinsed with PBS three times again. In order to perform nucleus labeling, the nuclei were stained with Hoechst 33324 solution (from Molecular Probes, 20 μg/mL in PBS, 1 mL/well) for 10 min. Then, the cells were rinsed with PBS three times. The coverslips were placed on a glass microscope slide, and the samples were visualized using CLSM (FV10-ASW).

Characterization. X-ray powder diffraction (XRD) measurements were performed on a Rigaku D/max-TTR-III diffractometer using Cu Kα radiation (λ = 0.15405 nm). SEM micrographs were obtained using a scanning electron microscope (SEM, JSM-6480A, Japan Electronics). Transmission electron microscopy (TEM) and high-resolution transmission electron microscopy (HRTEM) were recorded on a FEI Tecnai G^2 S-Twin with a field emission gun operating at 200 kV. Images were acquired digitally on a Gatan multiple CCD camera. Fourier transform IR (FT-IR) spectra were measured on a Perkin-Elmer 580B IR spectrophotometer. N_2 absorption/desorption isotherms were obtained at 77 K using a Micromeritics ASAP 2010 instrument. The specific surface area was calculated by the Brunauer−Emmett−Teller (BET) method. The pore size distribution was measured using the Barret−Joner−Halenda (BJH) method. UC emission spectra were obtained using 980 nm LD Module (K98D08M-30W, China) as the excitation source and detected by R955 (HAMAMATSU) from 400 to 900 nm. All the UC spectra in our experiment were gained under the same condition (980 nm laser diode with an excitation power density of 0.5 W cm^{-2}) with the same signal amplification. All the measurements were performed at room temperature.

RESULTS AND DISCUSSION

A detailed inspection of the as-synthesized 2D mesoporous structured MCM-41, MCM-41-Gd, and MCM-41-Gd@Au particles was carried out using TEM images (Figure 1). As

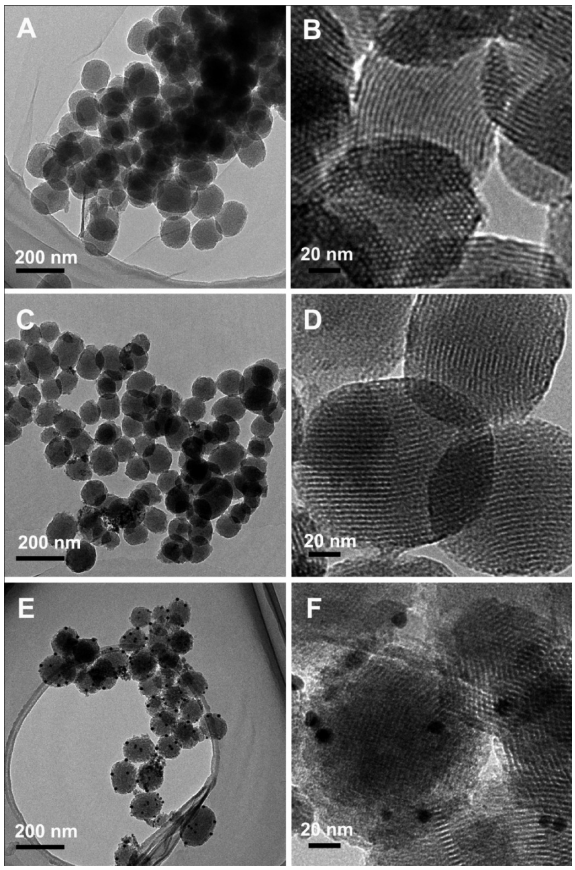

Figure 1. TEM images of (A, B) MCM-41, (C, D) MCM-41-Gd, and (E, F) MCM-41-Gd@Au.

shown, pure MCM-41 consists of uniform spherical nanoparticles with diameter of 80−100 nm (Figure 1A,B). The pore network exhibits linear hexagonal arrays of channels with excellent mesoscopic orders. During the synthesis process of MCM-41, Gd^{3+} was added and reacted with excess OH^-. After calcination at 800 °C for 4 h, the Gd_2O_3-assembled sample that is MCM-41-Gd was obtained (Figure 1C,D). No obvious

change is found in the particle size, morphology, and the mesoporous property from pure MCM-41 in the TEM images. The calculated size distribution of MCM-41-Gd and MCM-48-Gd is depicted in Figure S1, Supporting Information. About 300 particles were measured for the average particle size, which is 82.8 ± 1.9 nm. A small size distribution can be obtained. Moreover, the Gd_2O_3 clusters are totally assembled into the pore channels since no large Gd_2O_3 crystals are observed outside MCM-41-Gd particles or on the external surface. There exists a strong covalent bonding between Si of silica matrix and O of Gd_2O_3 molecule. Before hybridization with gold nanoparticles, the surface of MCM-41-Gd was first modified with an amino group, which provides strong coordination with the gold nanoparticles. As seen from MCM-41-Gd@Au (Figure 1E,F), the amino modification process has no side effect on the particle uniformity or aggregation, which could also be evidenced by the size distributions analysis (Figure S1, Supporting Information), and the gold nanoparticles are attached to the surface of MCM-41-Gd successfully without any free Au nanocrystals found nearby.

Similar examination of MCM-48, MCM-48-Gd, and MCM-48-Gd@Au was performed, and the TEM images are given in Figure 2. As shown, the size, shape, and structure of MCM-48-Gd are identical with those of pure MCM-48, which are composed of well-dispersed spherical particles with 3D cubic mesoporous structure (Figure 2A–D). Size distribution of MCM-48-Gd are depicted in Figure S1B, Supporting Information. The MCM-48-Gd sample also showed small size distribution; the average particle size is 214.5 ± 1.1 nm. From the TEM images of MCM-48-Gd@Au (Figure 2E,F), we can see that the gold nanoparticles are successfully attached onto the surface of MCM-48-Gd without any destruction of the mesopore structure. Low-angle XRD patterns of as-prepared MCM-41 and MCM-48 are presented in Figure S2, Supporting Information, which confirmed the respective mesostructure characteristics of both kinds of silica. Compared with pure MCM-41 and MCM-48, the characteristic peak positions of Gd assembled and Au coated samples shift slightly to a higher 2θ degree, and the corresponding intensities decrease a little, which can be attributed to the further condensation of Si–OH under proper heat treatment and inherent disorderness caused by the modification. Wide-angle XRD patterns of as-prepared MCM-41-Gd and MCM-48-Gd are also given in Figure S2, Supporting Information. However, no characteristics peaks of Gd_2O_3 crystalline structure can be detected. This result is similar to the report by Kleitz et al. about loading $GdSi_xO_y$ on MCM-48 and MCM-41,[59] which suggests the very fine size of the Gd_2O_3 clusters in our experiment, too small for being discriminated by XRD measurement.

Since the XRD analysis cannot give the trace of assembled Gd_2O_3 clusters, an EDS analysis on MCM-41-Gd@Au and MCM-48-Gd@Au was carried out to confirm the successful assembly of Gd_2O_3 into the mesoporous structure (Figure 3).

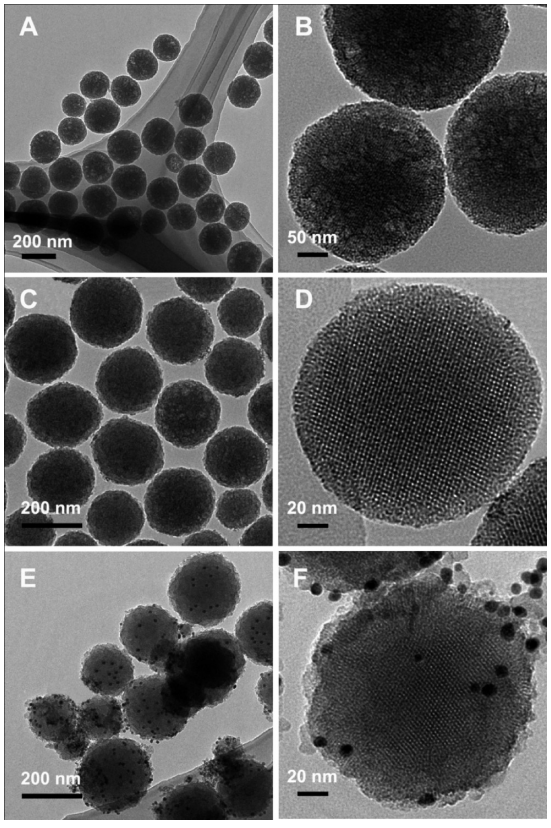

Figure 2. TEM images of (A, B) MCM-48, (C, D) MCM-48-Gd, and (E, F) MCM-48-Gd@Au.

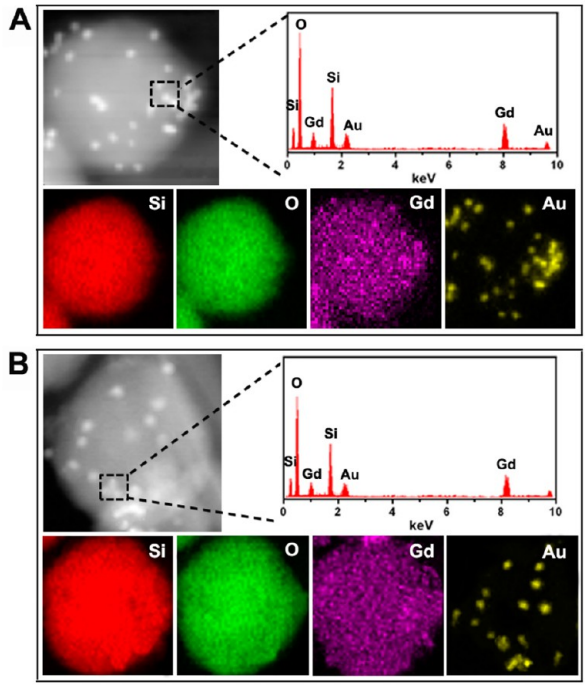

Figure 3. EDS spectra and mapping of (A) MCM-41-Gd@Au and (B) MCM-48-Gd@Au.

As seen, Gd, Si, O, and Au elements can be well detected in both samples. The gadolinium element is uniformly dispersed inside the silica porous network, and no gadolinium can be detected outside the mesoporous spheres. Moreover, the small gold crystals are also clear, which is on the surface of the silica spheres. The result is in good agreement with the above TEM analysis.

On the basis of the mesoporous structures of both kinds of materials, the nitrogen sorption behavior of MCM-41, MCM-41-Gd, MCM-41-Gd@Au, MCM-48, MCM-48-Gd, and MCM-48-Gd@Au was studied and depicted in Figure 4. As shown in Figure 4A, the MCM-41, MCM-41-Gd, and MCM-41-Gd@Au

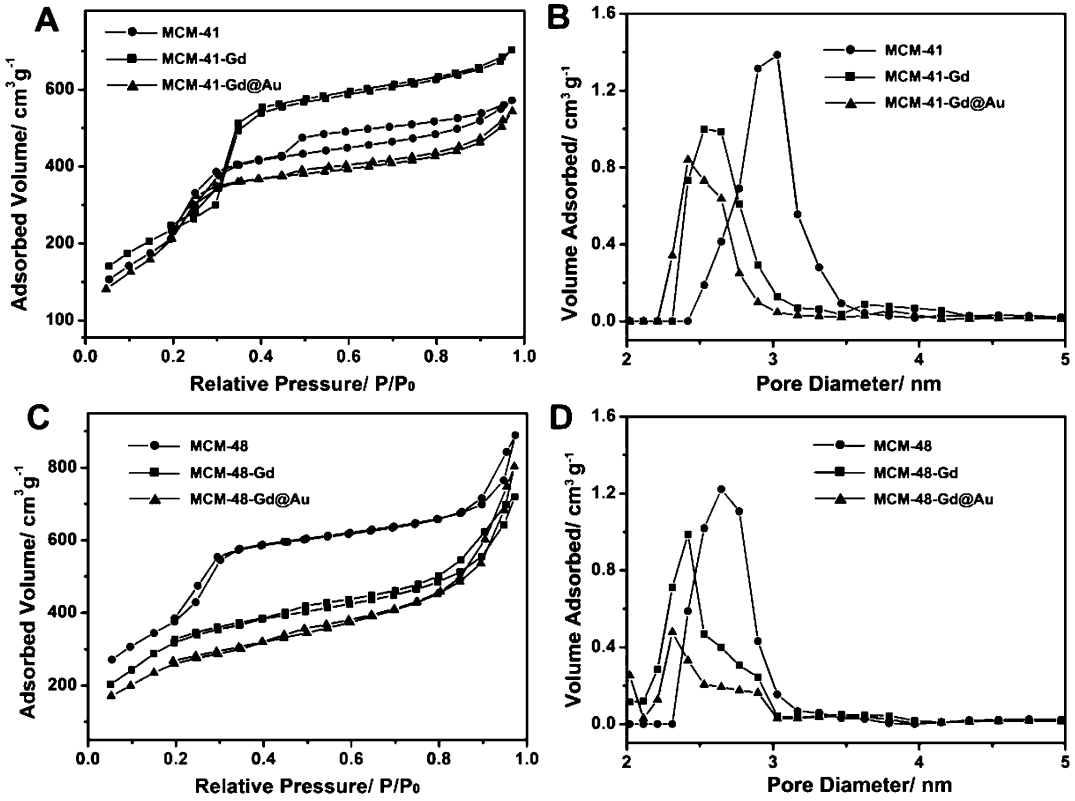

Figure 4. N_2 adsorption/desorption isotherms and pore size distribution of MCM-41, MCM-41-Gd, and MCM-41-Gd@Au (A, B) and MCM-48, MCM-48-Gd, and MCM-48-Gd @Au (C, D).

all exhibit IV-type isotherms, indicating the typical mesoporous structure for all three samples. For MCM-41-Gd, the assembly of Gd_2O_3 cluster does not change the basic pore structure of MCM-41. Moreover, the specific surface area, pore volume, and pore size of MCM-41-Gd were all decreased compared to those of pure MCM-41 (Figure 4A,B, Table 1), indicating that the pores are partially filled by the gadolinium oxide. Further hybrid of gold nanoparticles does not change the pore properties of MCM-41-Gd. Most importantly, despite the slight decrease, the pore parameters of MCM-41-Gd and MCM-41-Gd@Au remain relatively high, showing the good pore structure of these two samples. N_2 sorption results of MCM-48, MCM-48-Gd, and MCM-48-Gd@Au (Figure 4C,D) also confirmed the respective highly ordered mesostructures. Moreover, a slight decrease in the specific surface area, pore volume, and pore size is also found for MCM-48-Gd and MCM-48-Gd@Au due to the assembly of gadolinium oxide. The pore diameters for the 2D MCM-41 and 3D MCM-48 systems are close, whereas the specific surface areas and pore volumes of the MCM-48 system were noticeably higher than those of MCM-41 system (Table 1). Using the XRD unit cell parameter (α), we also calculated the wall thickness for the MCM-41 and MCM-48 systems, as depicted in Table 1.

Table 1. Textural Parameters of the Two Systems Extracted from N_2 Adsorption/Desorption Measurements and XRD Analysis[a]

samples	S_{BET} (m^2g^{-1})	D_p (nm)	V_p (cm^3g^{-1})	α (nm)	D_s (nm)
MCM-41	1241	3.030	0.989	4.429	1.399
MCM-41-Gd	961	2.531	0.837	4.047	1.516
MCM-41-Gd@Au	875	2.419	0.781	4.011	1.592
MCM-48	1688	2.647	1.196	8.128	1.417
MCM-48-Gd	1364	2.419	1.006	7.557	1.359
MCM-48-Gd@Au	1232	2.313	0.902	7.456	1.415

[a]For the MCM-41 system, $\alpha = d_{100}/3^{1/2}$, wall thickness $D_s = \alpha - D_p$ (pore size); for the MCM-48 system, $\alpha = 6^{1/2}d_{211}$, wall thickness $D_s = \alpha/2 - D_p$.

The UC luminescence spectra of MCM-41-Gd, MCM-41-Gd@Au, MCM-48-Gd, and MCM-48-Gd@Au under 980 nm LD excitation have been measured. (The doping concentrations are all 10% Yb^{3+} and 1% Er^{3+}.) As can be seen in Figure 5A,B, the spectra all exhibit clearly two green lines at about 525 and 545 nm and one red line at about 655 nm, which can be assigned to the $^2H_{11/2} \rightarrow {}^4I_{15/2}$, $^4S_{3/2} \rightarrow {}^4I_{15/2}$, and $^4F_{9/2} \rightarrow {}^4I_{15/2}$ transitions of Er^{3+} ions, respectively.[60] The population process for the three emissions has been reported a lot following the procedure below: $^4I_{15/2} \rightarrow {}^4I_{11/2} \rightarrow {}^4F_{7/2} \rightarrow {}^2H_{11/2}, {}^4S_{3/2}$ for the green emission and $^4I_{15/2} \rightarrow {}^4I_{11/2} \rightarrow {}^4I_{13/2} \rightarrow {}^4F_{9/2}$ for the red emission[61−69] (Figure 5D). It is well-known that attachment of the noble metal shell or nanostructures on the UC materials can affect the UC luminescence behaviors.[70,71] In this case, although the enhancement is not obvious in the UC spectra, through calculating the integrated peak area, we do find out that the emission intensities of MCM-41-Gd@Au and MCM-48-Gd@Au are increased compared to those of MCM-41-Gd and MCM-48-Gd samples. The enhancement factors for the green emission (520−560 nm), red emission (640−670 nm), and total emission intensities (520−670 nm) are calculated in Figure 5C. As can be seen, the UC intensities are enhanced for both green and red emissions, and the red emissions are enhanced more than the green emissions.

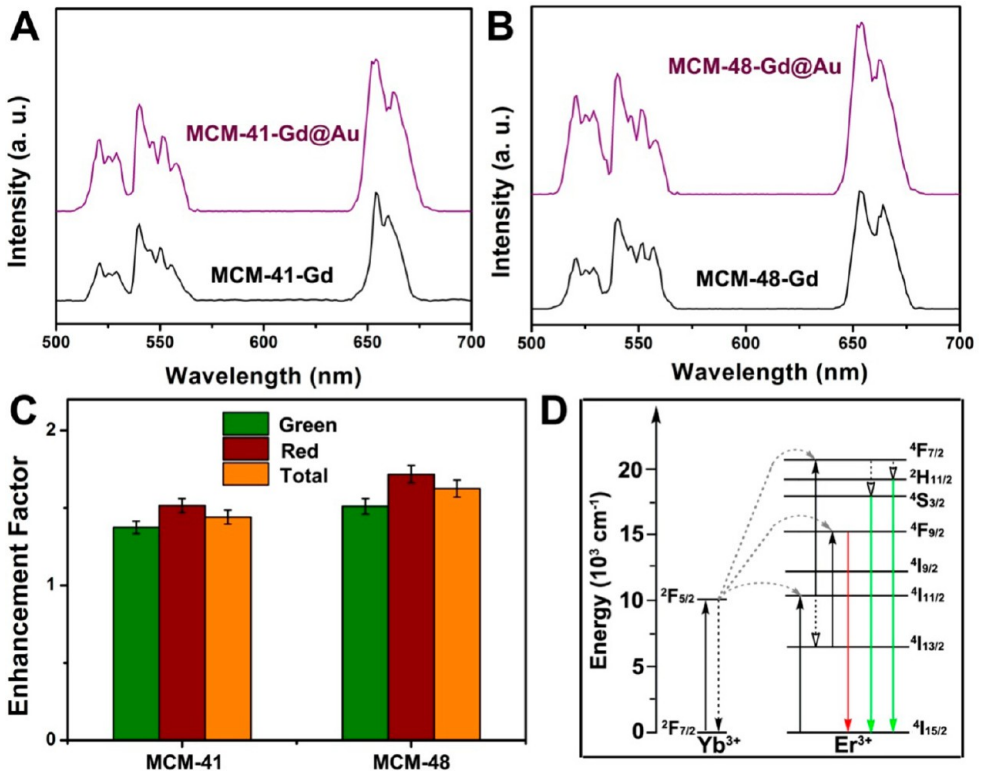

Figure 5. Comparison of UC luminescent spectra for (A) MCM-41-Gd and MCM-41-Gd@Au and (B) MCM-48-Gd and MCM-48-Gd@Au. (C) Enhancement factors of UC intensities for the two systems. (D) Energy state structure and energy transfer mechanisms of Yb^{3+} and Er^{3+}.

UC fluorescence properties of MCM-41-Gd@Au and MCM-48-Gd@Au with different MCM-41(48)-Gd/Au molar ratios have also been investigated. The plotting curves of the enhancement factor show an increasing trend with the MCM-41(48)-Gd/Au molar ratio increases from 1/1 to 4/1 and remain almost still when the MCM-41(48)-Gd/Au molar ratio is 6/1 (Figure 6A). Moreover, the green emissions of these hybrid crystals are enhanced less than the red emissions when the MCM-41(48)-Gd/Au molar ratio is increased, leading to a decrease of green/red intensity ratio (Figure 6B). This result confirmed that the UC enhancement caused by the attached Au nanoparticles is wavelength dependent. The luminescent photographs of MCM-41-Gd, MCM-41-Gd@Au, MCM-48-Gd, and MCM-41(48)-Gd/Au dispersed in water with MCM-41(48)-Gd/Au molar ratio of 4/1 are given in Figure 6A. The luminescence enhancement can be observed.

The enhancement of UC emissions can be explained by the surface plasmon resonance effect of attached gold nanocrystal, which has been reported metal before in quantum dots or fluorescent molecules.[72] First, the excitation flux rate can be enhanced caused by local field enhancement associated with plasmonic resonance. Second, the emission efficiency is increased due to the coupling of the UC emissions with the plasmonic resonance.[73] In our case, the gold nanoparticle attached samples have a strong plasmonic resonance band at around 550 nm (Figures S3 and S4, Supporting Information), which overlaps with the green emission in the UC spectra. Therefore, green up-conversion emissions will be absorbed more than the red emissions, which accounts for the wavelength-dependent enhancement factors.

Figure 7 exhibits the infrared thermal image of MCM-41-Gd, MCM-41-Gd@Au, MCM-48-Gd, and MCM-48-Gd@Au powders under 980 nm laser irradiation. The temperature of MCM-41-Gd and MCM-48-Gd powders increased to about 315 K under the laser irradiation, while the temperature of MCM-41-Gd@Au and MCM-48-Gd@Au increased to about 330 K under the same irradiation condition. The different temperature increases should be attributed to the photothermal effect of gold nanoparticles attached. This photothermal effect can be utilized during the drug release process. The detailed investigation will be given in the following drug release discussion.

For the loading of DOX molecules, the MCM-41-Gd (MCM-41-Gd@Au) or MCM-48-Gd (MCM-48-Gd@Au) was mixed with DOX for 24 h at room temperature. As shown in Figures S3 and S4, Supporting Information, after adsorption with DOX molecules, the color of MCM-41-Gd changes from white to orange, while MCM-41-Gd@Au changes from dark to light red. The UV–vis absorption spectrum of MCM-41(48)-Gd shows no absorption peak in the visible light region. After hybridization with gold nanoparticles, the absorption spectrum shows the plasma resonance peaks of Au nanoparticles at around 530 nm. All the DOX complex samples display the characteristic DOX absorption peak at 480 nm. Through measuring this characteristic absorption peak of DOX, the loading capacities of MCM-41-Gd, MCM-41-Gd@Au, MCM-48-Gd, and MCM-48-Gd@Au soaked with different concentrations of DOX are determined (Figure 8). The adsorption concentration increased with the increasing DOX concentration until the DOX amount was up to 2 mg/mL. Further increasing the initial DOX concentration to 3 mg/mL, the DOX loading content increases very little, meaning that further increase in DOX payload is not possible for this molecular adsorption. The adsorbed DOX of the MCM-48 system is a little higher than that of the MCM-41 system which may be due to the higher surface area and pore volume. For

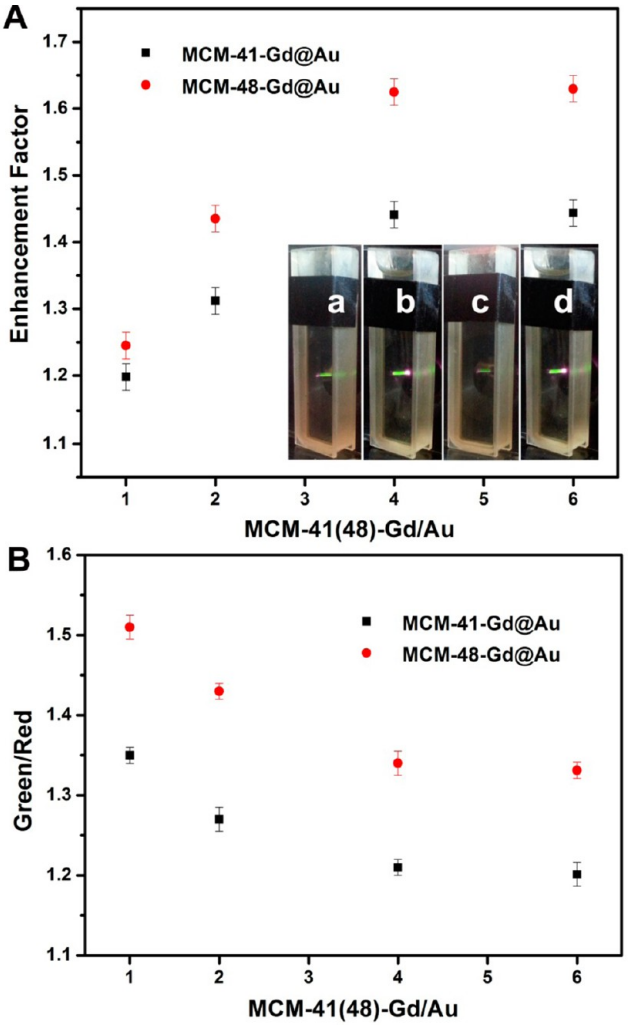

Figure 6. (A) Curve of plotting the UC luminescence enhancement factor with different MCM-41(48)-Gd/Au molar ratios (insets are the luminescent photographs for (a) MCM-41-Gd, (b) MCM-41-Gd@Au, (c) MCM-48-Gd, and (d) MCM-48-Gd@Au with MCM-41(48)-Gd/Au of 4). (B) Curve of plotting the intensity ratio between emission lines at 525 and 655 nm with different MCM-41(48)-Gd/Au molar ratios.

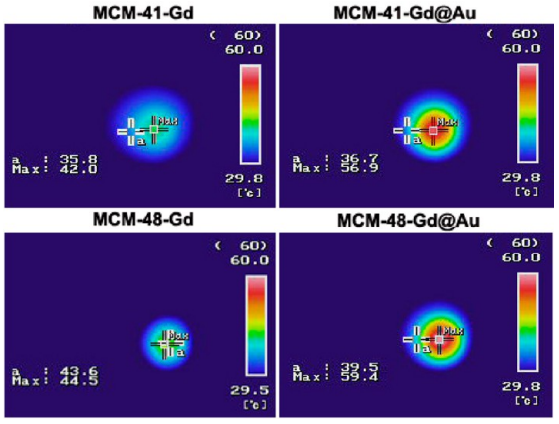

Figure 7. Infrared thermal image of MCM-41-Gd, MCM-41-Gd@Au, MCM-48-Gd, and MCM-48-Gd@Au powders under 980 nm laser irradiation with power density of 0.5 W/cm^2.

drug release experiments, the used DOX concentration is 2 mg/mL in the initial mixture, when the drug content adsorbed onto the silica systems was 78.98% and 73.23% for MCM-41-Gd and MCM-41-Gd@Au and 85.54% and 83.28% for MCM-48-Gd and MCM-48-Gd@Au, respectively. The high drug loading capability is attributed to the great physiochemical sorption caused by the large surface area of the mesoporous structure. It should be noted that the Au nanoparticle attached samples show a slight lower loading capacity to that of Au free samples (Figure 8B). FT-IR spectra of DOX loaded samples reveal the organic functional groups are attached on the surface of silica samples (Figure S5, Supporting Information).

The cumulative DOX release tests were first performed in PBS solution with pH value of 5.0. As for MCM-41-Gd and MCM-41-Gd@Au nanoparticles, the profiles all show a relatively slow and sustained release of DOX, which should be based on the interaction between DOX molecules and the mesopore structure (Figure 9A). The cumulative release reaches 30% in about 2 h and continuously rises to about 40% after 72 h. On the basis of the photothermal effect of gold nanoparticles under laser irradiation, we introduced a NIR light irradiation (980 nm, 0.5 W/cm^2) during the DOX release process. It can be clearly observed that the cumulative release of MCM-41-Gd@Au+DOX was obviously improved, which was about 19% higher than that without laser irradiation after 72 h. For comparison, the drug release test of MCM-41-Gd+DOX under the same irradiation was performed and does not show any change, meaning that the facilitation phenomenon is caused by the surface attached Au nanoparticles. Figure 10A shows the temperature plotting curves for pure PBS and DOX loaded MCM-41-Gd and MCM-41-Gd@Au in PBS as a function of laser irradiation time, respectively. The temperature of MCM-41-Gd@Au+DOX in PBS increased to about 43 °C after irradiation for about 10 min. It has been reported that, based on Au/Ag SPR induced by laser illumination, the local temperature can be increased, which is beneficial for drug release.[53,74,75] Herein, the MCM-41-Gd@Au nanoparticles have a strong SPR band at around 530 nm, which coincides with the UC green emission under 980 nm LD irradiation. Therefore, part of the laser can be absorbed by gold nanoparticles to cause their SPR and the local temperature increase. The thermal effect of as-prepared hybrid crystals exists in both powder (Figure 7) and solution conditions, and for the in vitro and in vivo experiments, luminescent labels and photothermal agents for bioapplications in living cells are always in aqueous states. The cancer cells can be killed when the temperature increases from body temperature (37 °C) to 43 °C, making our drug release system a good candicate in cancer therapy. The drug release profiles of MCM-48-Gd and MCM-48-Gd@Au are presented in Figure 9B, which are similar to that of the MCM-41 system. When a laser irradiation is presented, the cumulative release content of MCM-48-Gd@Au is about 17% improved than that without laser irradiation, confirming the laser irradiation can have a great effect on the drug release of gold nanoparticle attached sample. Furthermore, the thermal effect of MCM-48-Gd and MCM-48-Gd@Au in PBS was also measured (Figure 10B).

Another test of the effect of NIR laser irradiation on the MCM-41-Gd@Au drug release process was carried out when the release came to equilibrium in the dark and then continued under laser irradiation for another 10 h. As can be seen in Figure 9C, about 20% of the total drug is further released. These results indicate that the DOX release of the MCM-41-

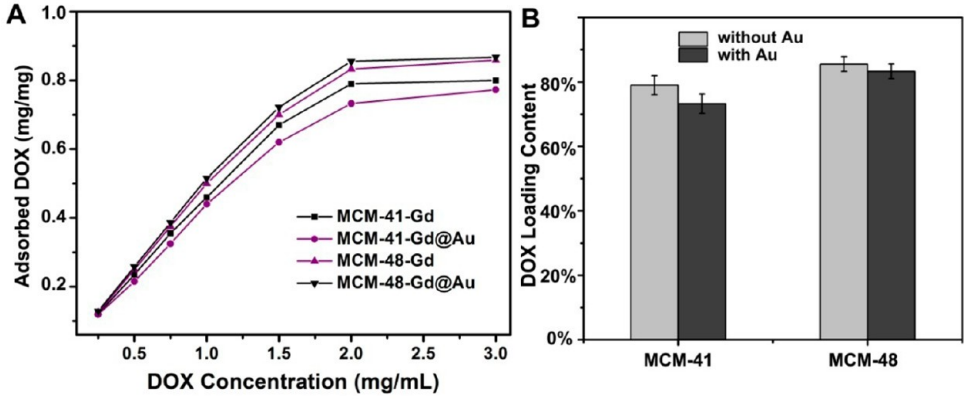

Figure 8. (A) DOX absorption curves showing the adsorption of DOX by MCM-41-Gd, MCM-41-Gd@Au, MCM-48-Gd, and MCM-48-Gd@Au with different DOX concentrations. (B) Comparison of DOX payload at the maximal DOX loading.

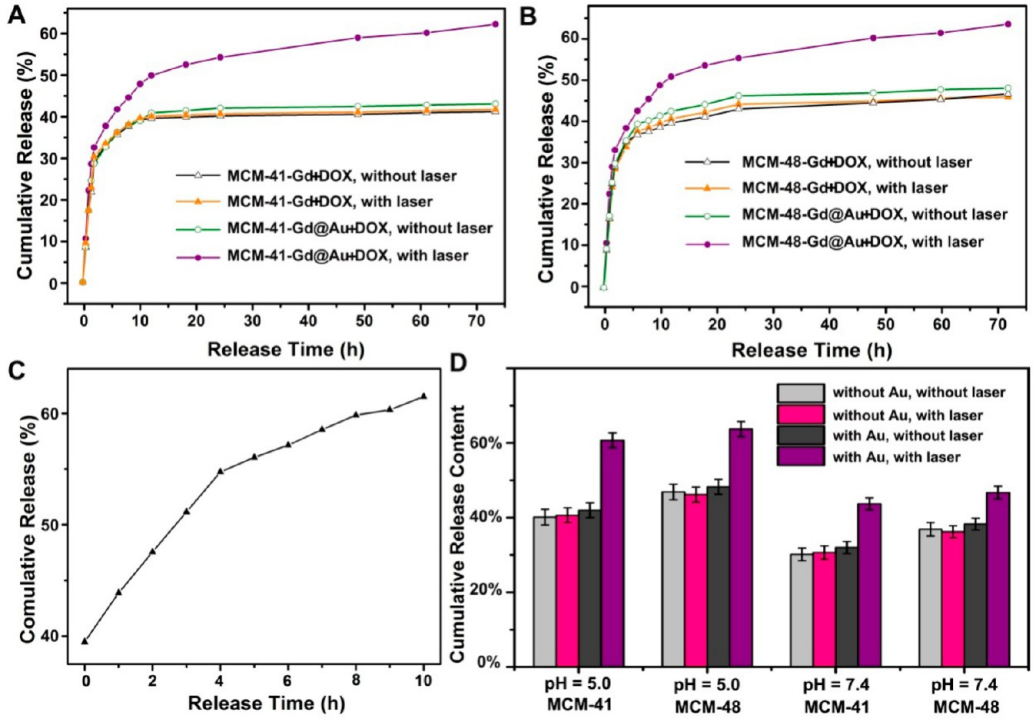

Figure 9. (A) Cumulative DOX release profile of MCM-41-Gd+DOX and MCM-41-Gd@Au+DOX with and without laser irradiation. (B) Further DOX release of MCM-41-Gd@Au with laser radiation after the release reached an equilibrium without laser irradiation. (C) Cumulative DOX release profile of MCM-48-Gd+DOX and MCM-48-Gd@Au+DOX with and without laser irradiation. (D) Comparison of the DOX release content.

Gd@Au system can readily be controlled by using the NIR laser. Furthermore, since the DOX molecules are attached to the mesoporous structures through electrostatic interaction, it can be deduced that the release of DOX would also be pH dependent. Therefore, we measured the drug release properties in PBS with pH value of 7.4. As shown in Figure 9D, the DOX release amount at pH 7.4 is significantly less than that in pH 5.0. This can be attributed to the dissociation of electrostatic interaction between positively charged DOX molecules and negatively charged silanols on the silica surface, based on the protonation of silanols at the decreased pH value.[51] The pH triggered drug release behavior of as-prepared samples makes them good candidates as smart carriers for releasing anticancer drug by changing the pH microenvironment from 7.4 (normal physiological environment) to 5.0 (acidic microenvironments, such as endosome and lysosome compartments). Furthermore, the Au nanocrystal attached samples show a much higher release rate under 980 nm light irradiation than that of the samples without irradiation.

The biocompatibility of as-prepared MCM-41-Gd@Au nanoparticles was measured using the standard MTT cell assay performed on human SKOV3 ovarian cancer (Figure 11). We can see that more than 100% of cell viabilities can be observed in a wide range of concentrations after incubation for 24 h (from 15.625 to 500 μg/mL), which indicates that the MCM-41-Gd@Au nanoparticles have no obvious cytotoxicity to SKOV3 cells, indicating that the nanoparticles have good biocompatibility as drug carriers in biomedical applications. This result indicates that the as-synthesized nanoparticles have good biocompatibility as drug carriers in biomedical applications.

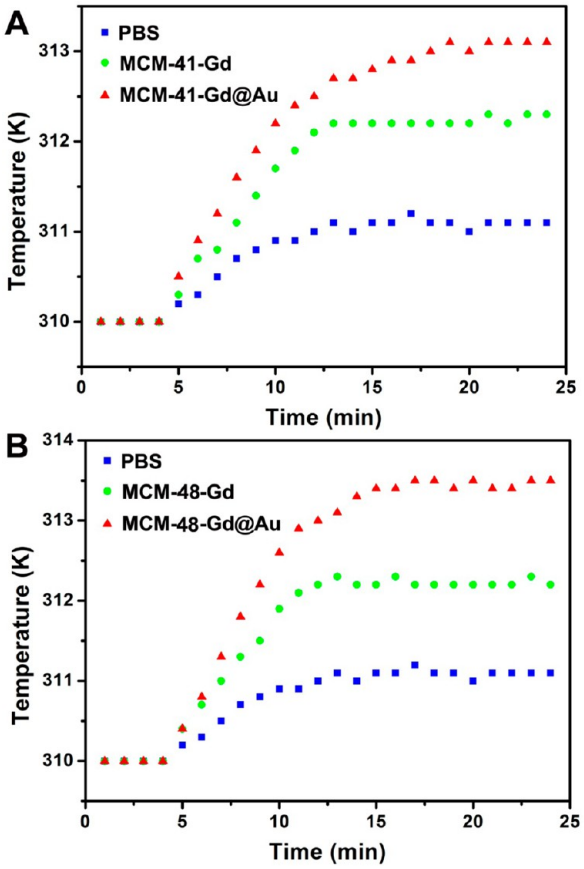

Figure 10. The temperature plotting curves of (A) PBS (pH = 5.0), MCM-41-Gd+DOX in PBS, and MCM-41@Au+DOX in PBS and (B) PBS (pH = 5.0), MCM-48-Gd+DOX in PBS, and MCM-48@Au +DOX in PBS as a function of laser irradiation time. (All the tests were performed in a 37 °C water bath.)

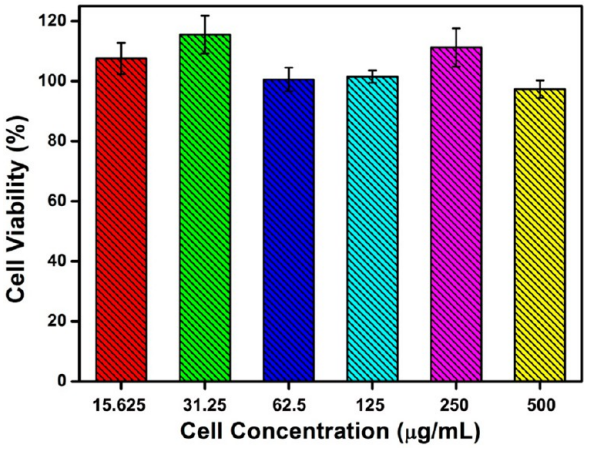

Figure 11. In vitro human SKOV3 ovarian cancer cells viability after incubating with MCM-41-Gd@Au nanoparticles for 24 h and quantitative assays by the standard MTT method.

The cytotoxic effect of MCM-41-Gd@Au+DOX against human SKOV3 ovarian cancer cells was evaluated in vitro via the MTT assay (Figure 12). First, free DOX molecule and MCM-41-Gd@Au+DOX with various concentrations were incubated in the human SKOV3 ovarian cancer cells for 24 h. (The concentration of free DOX was set as the same as the MCM-41-Gd@Au+DOX.) As can be seen from Figure 12A,B, both samples exhibit an increasing inhibition against human SKOV3 ovarian cancer cells along with the concentration increasing. Free DOX molecules can be diffused into cells much faster than the nanoparticles, since the nanoparticles have to enter the cancer cells through endocytic effect. Thus, with the same DOX concentration, free DOX tends to kill more cells. When the concentration is higher, more and more DOX conjugated nanoparticles can be endocytosed to enter the cancer cells and release DOX inside to induce cell death. This result indicates that the released DOX from MCM-41-Gd@Au +DOX nanoparticles is pharmacologically active. On the other hand, based on the hyperthermia effect of gold nanoparticles, we measured the cell viability of MCM-41-Gd@Au and MCM-41-Gd@Au+DOX incubated prior to laser irradiation of 10 min. As shown in Figure 12C,D, treatment with NIR light resulted in an increased inhibition of cell viability compared to that without light treatment.

In order to verify the cell uptake process, the CLSM photographs of human SKOV3 ovarian cancer cells incubated with as-prepared MCM-41-Gd@Au+DOX for 30 min and 3 h at 37 °C were taken. As shown in Figure 13, each series can be classified into the nuclei of cells (dyed blue by Hoechst 33324 for visualization), MCM-41-Gd@Au+DOX, and a mergence of the two channels of both above, respectively. The excitation wavelengths of Hoechst 33324 and DOX are 405 and 543 nm, respectively, and the red emission (572 nm) is derived from DOX molecular. In the first 30 min, only a few of the composites were taken up by SKOV3 cells. With the increase of the incubation time to 3 h, more nanoparticles have crossed the membrane and are localized in the cytoplasm. The red fluorescence of DOX was observed in both the cytoplasm and the cell nucleus. Through the time course CLSM result, it can be concluded that as-prepared samples can be effectively taken up by SKOV3 cells. The intracellular pathway of the MCM-41-Gd@Au+DOX particles comprised rapid internalization, nanoparticle localization in the endocytic compartments, and fast release DOX in the acid microenvironment.

CONCLUSION

In summary, a one-step synthesis of gadolinium-assembled mesoporous MCM-41-Gd and MCM-48-Gd nanocomposites was reported. The as-prepared MCM-41-Gd with 2D hexagonal pore network and MCM-48-Gd with 3D cubic pore network all present good UC luminescence. Then, gold nanocrystals with diameter of 5 nm were integrated onto the surface of MCM-41-Gd and MCM-48-Gd, which induced a wavelength-dependent enhancement of the UC intensities. DOX loading and release tests in the two systems reveal the high potential in the drug delivery field. Under 980 nm NIR laser irradiation, the photothermal effect of gold nanocrystals was triggered and induced a rapid DOX release from the Au hybrid materials. This laser triggered rapid drug release was also confirmed in different pH conditions. Meanwhile, the cytotoxic effect and photothermal theatment of MCM-41-Gd@Au+DOX were observed obviously on SKOV3 ovarian cancer cells via MTT assay. The cell uptake process was also confirmed through CLSM cell images. Such novel anticancer drug delivery systems, which combined multifunctional properties (mesoporous, UC luminescence, photothermal effect), should have potential application in cancer therapy.

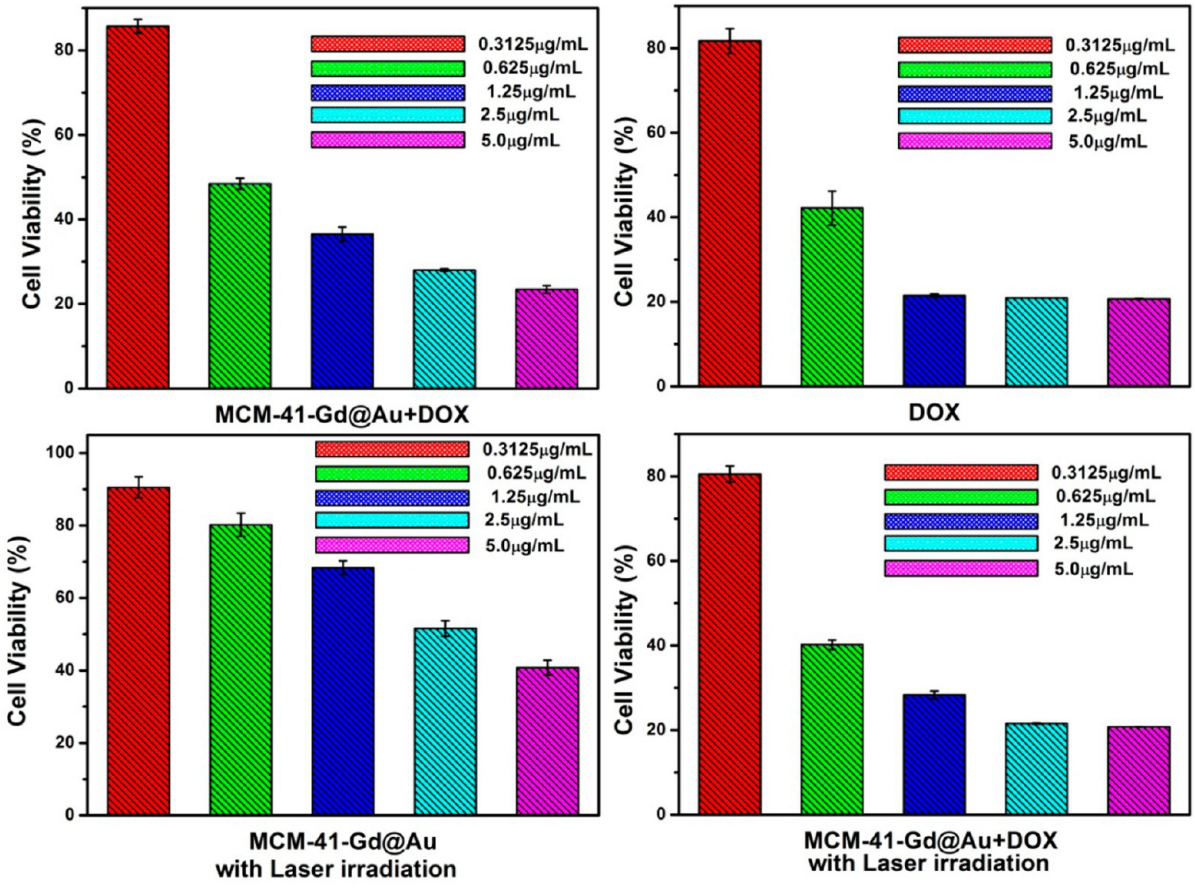

Figure 12. In vitro human SKOV3 ovarian cancer cell viabilities after incubation with MCM-41-Gd@Au+DOX, free DOX, MCM-41-Gd@Au with laser irradiation (0.5 W/cm^2), and MCM-41-Gd@Au+DOX with laser irradiation (0.5 W/cm^2).

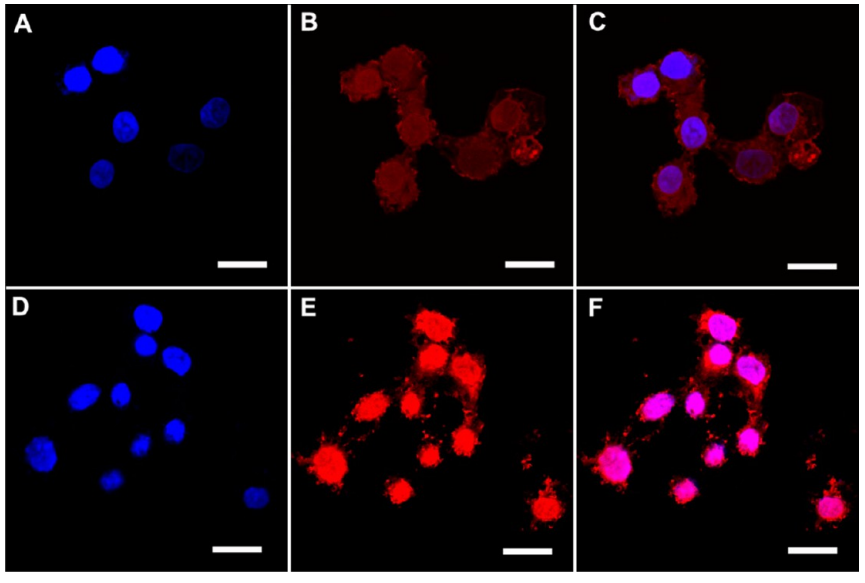

Figure 13. Confocal laser scanning microscopy (CLSM) images of human SKOV3 ovarian cancer cells incubated with MCM-41-Gd@Au+DOX for 30 min (A–C) and 3 h (D–F) at 37 °C. Scale bars for all images are 50 μm.

■ ASSOCIATED CONTENT

Supporting Information

Size distributions, XRD analysis, absorption spectra, and FT-IR spectra for the two systems. This material is available free of charge via the Internet at http://pubs.acs.org.

■ AUTHOR INFORMATION

Corresponding Authors

*E-mail: yangpiaoping@hrbeu.edu.cn.
*E-mail: qufengyuchem@yahoo.com.cn.

Notes

The authors declare no competing financial interest.

■ ACKNOWLEDGMENTS

Financial support from the National Natural Science Foundation of China (NSFC 21271053, 21170145), Research Fund for the Doctoral Program of Higher Education of China (20112304110021), Natural Science Foundation of Heilongjiang Province (LC2012C10), Program for New Century Excellent Talents in University, Harbin Sci.-Tech. Innovation Foundation (RC2012XK017012), and the Fundamental Research Funds for the Central Universities of China is greatly acknowledged.

■ REFERENCES

(1) Yang, P.; Gai, S.; Lin, J. Functionalized Mesoporous Silica Materials for Controlled Drug Delivery. *Chem. Soc. Rev.* **2012**, *41*, 3679−3698.
(2) Li, Z.; Barnes, J. C.; Bosoy, A.; Stoddart, J. F.; Zink, J. I. Mesoporous Silica Nanoparticles in Biomedical Applications. *Chem. Soc. Rev.* **2012**, *41*, 2590−2605.
(3) Liu, J.; Bu, W.; Pan, L.; Shi, J. NIR-Triggered Anticancer Drug Delivery by Upconverting Nanoparticles with Integrated Azobenzene-Modified Mesoporous Silica. *Angew. Chem., Int. Ed.* **2013**, *52*, 4375−4379.
(4) Lin, Q. N.; Bao, C. Y.; Yang, Y. L.; Liang, Q. N.; Zhang, D. S.; Cheng, S. Y.; Zhu, L. Y. Highly Discriminating Photorelease of Anticancer Drugs Based on Hypoxia Activatable Phototrigger Conjugated Chitosan Nanoparticles. *Adv. Mater.* **2013**, *25*, 1981−1986.
(5) Stark, W. J. Nanoparticles in Biological Systems. *Angew. Chem., Int. Ed.* **2011**, *50*, 1242−1258.
(6) Wang, C.; Tao, H.; Cheng, L.; Liu, Z. Near-Infrared Light Induced in vivo Photodynamic Therapy of Cancer Based on Upconversion Nanoparticles. *Biomaterials* **2011**, *32*, 6145−6154.
(7) Jain, T. K.; Morales, M. A.; Sahoo, S. K.; Leslie-Pelecky, D. L.; Labhasetwar, V. Iron Oxide Nanoparticles for Sustained Delivery of Anticancer Agents. *Mol. Pharmacol.* **2005**, *2*, 194−205.
(8) Liu, Z.; Chen, K.; Davis, C.; Sherlock, S.; Cao, Q.; Chen, X.; Dai, H. Drug Delivery with Carbon Nanotubes for in vivo Cancer Treatment. *Cancer Res.* **2008**, *68*, 6652−6660.
(9) Fang, Y.; Gu, D.; Zou, Y.; Wu, Z. X.; Li, F. Y.; Che, R. C.; Deng, Y. H.; Tu, B.; Zhao, D. Y. A Low-Concentration Hydrothermal Synthesis of Biocompatible Ordered Mesoporous Carbon Nanospheres with Tunable and Uniform Size. *Angew. Chem., Int. Ed.* **2010**, *49*, 7987−7991.
(10) Wang, C.; Cheng, L. A.; Liu, Z. A. Drug Delivery with Upconversion Nanoparticles for Multi-functional Targeted Cancer Cell Imaging and Therapy. *Biomaterials* **2011**, *32*, 1110−1120.
(11) Dai, Y.; Yang, D.; Ma, P. A.; Kang, X.; Zhang, X.; Li, C.; Hou, Z.; Cheng, Z.; Lin, J. Doxorubicin Conjugated $NaYF_4$:Yb^{3+}/Tm^{3+} Nanoparticles for Therapy and Sensing of Drug Delivery by Luminescence Resonance Energy Transfer. *Biomaterials* **2012**, *33*, 8704−8713.
(12) Tu, D. T.; Liu, L. Q.; Ju, Q.; Liu, Y. S.; Zhu, H. M.; Li, R. F.; Chen, X. Y. Time-Resolved FRET Biosensor Based on Amine-Functionalized Lanthanide-Doped $NaYF_4$ Nanocrystals. *Angew. Chem., Int. Ed.* **2011**, *50*, 6306−6310.
(13) Liu, F. Y.; He, X. X.; Liu, L.; You, H. P.; Zhang, H. M.; Wang, Z. X. Conjugation of $NaGdF_4$ Upconverting Nanoparticles on Silica Nanospheres as Contrast Agents for Multi-Modality Imaging. *Biomaterials* **2013**, *34*, 5218−5225.
(14) You, J.; Zhang, G. D.; Li, C. Exceptionally High Payload of Doxorubicin in Hollow Gold Nanospheres for Near-Infrared Light-Triggered Drug Release. *ACS Nano* **2010**, *4*, 1033−1041.
(15) Giri, S.; Trewyn, B. G.; Stellmaker, M. P.; Lin, V. S. Y. Stimuli-Responsive Controlled-Release Delivery System Based on Mesoporous Silica Nanorods Capped with Magnetic Nanoparticles. *Angew. Chem., Int. Ed.* **2005**, *44*, 5038−5044.
(16) Lin, Q. N.; Huang, Q.; Li, C. Y.; Bao, C. Y.; Liu, Z. Z.; Li, F. Y.; Zhu, L. Y. Anticancer Drug Release from a Mesoporous Silica Based Nanophotocage Regulated by Either a One- or Two-Photon Process. *J. Am. Chem. Soc.* **2010**, *132*, 10645−10647.
(17) Kim, J.; Lee, J. E.; Lee, S. H.; Yu, J. H.; Lee, J. H.; Park, T. G.; Hyeon, T. Designed Fabrication of a Multifunctional Polymer Nanomedical Platform for Simultaneous Cancer-Targeted Imaging and Magnetically Guided Drug Delivery. *Adv. Mater.* **2008**, *20*, 478−483.
(18) Zhao, W. R.; Gu, J. L.; Zhang, L. X.; Chen, H. R.; Shi, J. L. Fabrication of Uniform Magnetic Nanocomposite Spheres with a Magnetic Core/Mesoporous Silica Shell Structure. *J. Am. Chem. Soc.* **2005**, *127*, 8916−8917.
(19) Gai, S. L.; Yang, P. P.; Li, C. X.; Wang, W. X.; Dai, Y. L.; Niu, N.; Lin, J. Synthesis of Magnetic, Up-Conversion Luminescent, and Mesoporous Core-Shell-Structured Nanocomposites as Drug Carriers. *Adv. Funct. Mater.* **2010**, *20*, 1166−1172.
(20) Kim, T. W.; Chung, P. W.; Lin, V. S. Y. Facile Synthesis of Monodisperse Spherical MCM-48 Mesoporous Silica Nanoparticles with Controlled Particle Size. *Chem. Mater.* **2010**, *22*, 5093−5104.
(21) Barbe, C.; Bartlett, J.; Kong, L. G.; Finnie, K.; Lin, H. Q.; Larkin, M.; Calleja, S.; Bush, A.; Calleja, G. Silica Particles: A Novel Drug-Delivery System. *Adv. Mater.* **2004**, *16*, 1959−1966.
(22) Liu, J.; Bu, W.; Zhang, S.; Chen, F.; Xing, H.; Pan, L.; Zhou, L.; Peng, W.; Shi, J. Controlled Synthesis of Uniform and Monodisperse Upconversion Core/Mesoporous Silica Shell Nanocomposites for Bimodal Imaging. *Chem.—Eur. J.* **2012**, *18*, 2335−2341.
(23) Vallet-Regi, M.; Balas, F.; Arcos, D. Mesoporous Materials for Drug Delivery. *Angew. Chem., Int. Ed.* **2007**, *46*, 7548−7558.
(24) Yang, P. P.; Quan, Z. W.; Li, C. X.; Lian, H. Z.; Huang, S. S.; Lin, J. Fabrication, Characterization of Spherical $CaWO_4$:Ln@MCM-41 (Ln = Eu^{3+}, Dy^{3+}, Sm^{3+}, Er^{3+}) Composites and Their Applications as Drug Release Systems. *Microporous Mesoporous Mater.* **2008**, *116*, 524−531.
(25) Li, Y. J.; Yan, B.; Wang, L. Rare Earth (Eu^{3+}, Tb^{3+}) Mesoporous Hybrids with Calix 4 Arene Derivative Covalently Linking MCM-41: Physical Characterization and Photoluminescence Property. *J. Solid State Chem.* **2011**, *184*, 2571−2579.
(26) Cheng, L.; Yang, K.; Li, Y. G.; Zeng, X.; Shao, M. W.; Lee, S.-T.; Liu, Z. Multifunctional Nanoparticles for Upconversion Luminescence/MR Multimodal Imaging and Magnetically Targeted Photothermal Therapy. *Biomaterials* **2012**, *33*, 2215−2222.
(27) Cheng, L.; Yang, K.; Li, Y. G.; Chen, J. H.; Wang, C.; Shao, M. W.; Lee, S.-T.; Liu, Z. Facile Preparation of Multifunctional Upconversion Nanoprobes for Multimodal Imaging and Dual-Targeted Photothermal Therapy. *Angew. Chem., Int. Ed.* **2011**, *50*, 7385−7390.
(28) Wong, H. T.; Chan, H. L. W.; Hao, J. H. Towards Pure Near-Infrared to Near-Infrared Upconversion of Multifunctional GdF_3:Yb^{3+},Tm^{3+} Nanoparticles. *Opt. Express* **2010**, *18*, 6123−6130.
(29) Liu, Y. X.; Wang, D. S.; Shi, J. X.; Peng, Q.; Li, Y. D. Magnetic Tuning of Upconversion Luminescence in Lanthanide-Doped Bifunctional Nanocrystals. *Angew. Chem., Int. Ed.* **2013**, *52*, 4366−4369.
(30) Kumar, R.; Nyk, M.; Ohulchanskyy, T. Y.; Flask, C. A.; Prasad, P. N. Combined Optical and MR Bioimaging Using Rare Earth Ion Doped $NaYF_4$ Nanocrystals. *Adv. Funct. Mater.* **2009**, *19*, 853−859.
(31) Diamente, P. R.; Raudsepp, M.; van Veggel, F. C. J. M. Dispersible Tm^{3+}-Doped Nanoparticles that Exhibit Strong 1.47 μm Photoluminescence. *Adv. Funct. Mater.* **2007**, *17*, 363−368.
(32) Zhang, Q.; Yan, B. Phase Control of Upconversion Nanocrystals and New Rare Earth Fluorides though a Diffusion-Controlled Strategy in a Hydrothermal System. *Chem. Commun.* **2011**, *47*, 5867−5869.
(33) Li, Z. Q.; Zhang, Y. Monodisperse Silica-Coated Polyvinylpyrrolidone/$NaYF_4$ Nanocrystals with Multicolor Upconversion Fluorescence Emission. *Angew. Chem., Int. Ed.* **2006**, *45*, 7732−7735.
(34) Hou, Z. Y.; Li, C. X.; Ma, P. A.; Cheng, Z. Y.; Li, X. J.; Zhang, X.; Dai, Y. L.; Yang, D. M.; Lian, H. Z.; Lin, J. Up-Conversion Luminescent and Porous $NaYF_4$:Yb^{3+},Er^{3+}@SiO_2 Nanocomposite

Fibers for Anti-Cancer Drug Delivery and Cell Imaging. *Adv. Funct. Mater.* **2012**, *22*, 2713−2722.
(35) Shao, Y. Z.; Tian, X. M.; Hu, W. Y.; Zhang, Y. Y.; Liu, H.; He, H. Q.; Shen, Y. Y.; Xie, F. K.; Li, L. The Properties of Gd_2O_3-Assembled Silica Nanocomposite Targeted Nanoprobes and Their Application in MRI. *Biomaterials* **2012**, *33*, 6438−6446.
(36) Wang, Y. F.; Sun, L. D.; Xiao, J. W.; Feng, W.; Zhou, J. C.; Shen, J.; Yan, C. H. Rare-Earth Nanoparticles with Enhanced Upconversion Emission and Suppressed Rare-Earth-Ion Leakage. *Chem.—Eur. J.* **2012**, *18*, 5558−5564.
(37) Wang, F.; Banerjee, D.; Liu, Y. S.; Chen, X. Y.; Liu, X. G. Upconversion Nanoparticles in Biological Labeling, Imaging, and Therapy. *Analyst* **2010**, *135*, 1839−1854.
(38) Su, Q. Q.; Han, S. Y.; Xie, X. J.; Zhu, H. M.; Chen, H. Y.; Chen, C. K.; Liu, R. S.; Chen, X. Y.; Wang, F.; Liu, X. G. The Effect of Surface Coating on Energy Migration-Mediated Upconversion. *J. Am. Chem. Soc.* **2012**, *134*, 20849−20857.
(39) Wang, Z. L.; Hao, J. H.; Chan, H. L. W.; Wong, W. T.; Wong, K. L. A Strategy for Simultaneously Realizing the Cubic-to-Hexagonal Phase Transition and Controlling the Small Size of $NaYF_4$:Yb^{3+},Er^{3+} Nanocrystals for In Vitro Cell Imaging. *Small* **2012**, *8*, 1863−1868.
(40) Chen, Z. G.; Chen, H. L.; Hu, H.; Yu, M. X.; Li, F. Y.; Zhang, Q.; Zhou, Z. G.; Yi, T.; Huang, C. H. Versatile Synthesis Strategy for Carboxylic Acid-Functionalized Upconverting Nanophosphors as Biological Labels. *J. Am. Chem. Soc.* **2008**, *130*, 3023−3029.
(41) Wang, G. F.; Peng, Q.; Li, Y. D. Lanthanide-Doped Nanocrystals: Synthesis, Optical-Magnetic Properties, and Applications. *Acc. Chem. Res.* **2011**, *44*, 322−332.
(42) Liu, F. Y.; Zhao, Q.; You, H. P.; Wang, Z. X. Synthesis of Stable Carboxy-Terminated $NaYF_4$:Yb^{3+},Er^{3+}@SiO_2 Nanoparticles with Ultrathin Shell for Biolabeling Applications. *Nanoscale* **2013**, *5*, 1047−1053.
(43) Yang, P. P.; Quan, Z. W.; Hou, Z. Y.; Li, C. X.; Kang, X. J.; Cheng, Z. Y.; Lin, J. A Magnetic, Luminescent and Mesoporous Core-Shell Structured Composite Material as Drug Carrier. *Biomaterials* **2009**, *30*, 4786−4795.
(44) Yang, P. P.; Quan, Z. W.; Lu, L. L.; Huang, S. S.; Lin, J. Luminescence Functionalization of Mesoporous Silica with Different Morphologies and Applications as Drug Delivery Systems. *Biomaterials* **2008**, *29*, 692−702.
(45) Yang, G.; Gai, S.; Qu, F.; Yang, P. SiO_2@YBO_3:Eu^{3+} Hollow Mesoporous Spheres for Drug Delivery Vehicle. *ACS Appl. Mater. Interfaces* **2013**, *5*, 5788−5796.
(46) Dong, B. A.; Xu, S.; Sun, J. A.; Bi, S.; Li, D.; Bai, X.; Wang, Y.; Wang, L. P.; Song, H. W. Multifunctional $NaYF_4$:Yb^{3+},Er^{3+}@Ag Core/Shell Nanocomposites: Integration of Upconversion Imaging and Photothermal Therapy. *J. Mater. Chem.* **2011**, *21*, 6193−6200.
(47) Fujii, M.; Nakano, T.; Imakita, K.; Hayashi, S. Upconversion Luminescence of Er and Yb Codoped $NaYF_4$ Nanoparticles with Metal Shells. *J. Phys. Chem. C* **2013**, *117*, 1113−1120.
(48) Zhang, F.; Braun, G. B.; Shi, Y. F.; Zhang, Y. C.; Sun, X. H.; Reich, N. O.; Zhao, D. Y. Stucky, Fabrication of Ag@SiO_2@Y_2O_3:Er Nanostructures for Bioimaging: Tuning of the Upconversion Fluorescence with Silver Nanoparticles. *J. Am. Chem. Soc.* **2010**, *132*, 2850−2851.
(49) Li, Z. Q.; Wang, L. M.; Wang, Z. Y.; Liu, X. H.; Xiong, Y. J. Modification of $NaYF_4$:Yb,Er@SiO_2 Nanoparticles with Gold Nanocrystals for Tunable Green-to-Red Upconversion Emissions. *J. Phys. Chem. C* **2011**, *115*, 3291−3296.
(50) Xu, B. B.; Chen, P.; Zhou, S. F.; Hong, Z. L.; Hao, J. H.; Qiu, J. R. Enhanced Broadband Near-Infrared Luminescence in Bi-doped Glasses by Co-Doping with Ag. *J. Appl. Phys.* **2013**, *113*, 183506-1−183506-5.
(51) Feng, W.; Sun, L.-D.; Yan, C.-H. Ag Nanowires Enhanced Upconversion Emission of $NaYF_4$:Yb,Er Nanocrystals via a Direct Assembly Method. *Chem. Commun.* **2009**, 4393−4395.
(52) Wang, L.; Yan, R.; Huo, Z.; Wang, L.; Zeng, J.; Bao, J.; Wang, X.; Peng, Q.; Li, Y. Fluorescence Resonant Energy Transfer Biosensor Based on Upconversion-Luminescent Nanoparticles. *Angew. Chem., Int. Ed.* **2005**, *44*, 6054−6057.
(53) Chen, Y.; Chen, H. R.; Zeng, D. P.; Tian, Y. B.; Chen, F.; Feng, J. W.; Shi, J. L. C Core/Shell Structured Hollow Mesoporous Nanocapsules: A Potential Platform for Simultaneous Cell Imaging and Anticancer Drug Delivery. *ACS Nano* **2010**, *4*, 6001−6013.
(54) Kang, H. Z.; Trondoli, A. C.; Zhu, G. Z.; Chen, Y.; Chang, Y. J.; Liu, H. P.; Huang, Y. F.; Zhang, X. L.; Tan, W. H. Near-Infrared Light-Responsive Core-Shell Nanogels for Targeted Drug Delivery. *ACS Nano* **2011**, *5*, 5094−5099.
(55) Ma, M.; Chen, H. R.; Chen, Y.; Wang, X.; Chen, F.; Cui, X. Z.; Shi, J. L. Au Capped Magnetic Core/Mesoporous Silica Shell Nanoparticles for Combined Photothermo-/Chemo-Therapy and Multimodal Imaging. *Biomaterials* **2012**, *33*, 989−998.
(56) Zhang, Z. J.; Wang, L. M.; Wang, J.; Jiang, X. M.; Li, X. H.; Hu, Z. J.; Ji, Y. H.; Wu, X. C.; Chen, C. Y. Mesoporous Silica-Coated Gold Nanorods as a Light-Mediated Multifunctional Theranostic Platform for Cancer Treatment. *Adv. Mater.* **2012**, *24*, 1418−1423.
(57) Lai, C.-Y.; Trewyn, B. G.; Jeftinija, D. M.; Jeftinija, K.; Xu, S.; Jeftinija, S.; Lin, V. S. Y. A Mesoporous Silica Nanosphere-Based Carrier System with Chemically Removable CdS Nanoparticle Caps for Stimuli-Responsive Controlled Release of Neurotransmitters and Drug Molecules. *J. Am. Chem. Soc.* **2003**, *125*, 4451−4459.
(58) Kim, T.-W.; Chung, P.-W.; Slowing, I. I.; Tsunoda, M.; Yeung, E. S.; Lin, V. S. Y. Structurally Ordered Mesoporous Carbon Nanoparticles as Transmembrane Delivery Vehicle in Human Cancer Cells. *Nano Lett.* **2008**, *8*, 3724−3727.
(59) Guillet-Nicolas, R.; Bridot, J. L.; Seo, Y.; Fortin, M. A.; Kleitz, F. Enhanced Relaxometric Properties of MRI "Positive" Contrast Agents Confined in Three-Dimensional Cubic Mesoporous Silica Nanoparticles. *Adv. Funct. Mater.* **2011**, *21*, 4653−4662.
(60) Hao, J. H.; Zhang, Y.; Wei, X. H. Electric-Induced Enhancement and Modulation of Upconversion Photoluminescence in Epitaxial $BaTiO_3$:Yb/Er Thin Films. *Angew. Chem., Int. Ed.* **2011**, *50*, 6876−6880.
(61) Heer, S.; Kompe, K.; Gudel, H. U.; Haase, M. Highly Efficient Multicolour Upconversion Emission in Transparent Colloids of Lanthanide-Doped $NaYF_4$ Nanocrystals. *Adv. Mater.* **2004**, *16*, 2102−2105.
(62) Li, C. X.; Lin, J. Rare Earth Fluoride Nano-/Microcrystals: Synthesis, Surface Modification and Application. *J. Mater. Chem.* **2010**, *20*, 6831−6847.
(63) Mai, H. X.; Zhang, Y. W.; Sun, L. D.; Yan, C. R. Size- and Phase-Controlled Synthesis of Monodisperse $NaYF_4$:Yb,Er Nanocrystals from a Unique Delayed Nucleation Pathway Monitored with Upconversion Spectroscopy. *J. Phys. Chem. C* **2007**, *111*, 13730−13739.
(64) Wang, F.; Liu, X. G. Recent Advances in the Chemistry of Lanthanide-Doped Upconversion Nanocrystals. *Chem. Soc. Rev.* **2009**, *38*, 976−989.
(65) Wang, L. Y.; Li, Y. D. Controlled Synthesis and Luminescence of Lanthanide Doped $NaYF_4$ Nanocrystals. *Chem. Mater.* **2007**, *19*, 727−734.
(66) Yi, G. S.; Chow, G. M. Synthesis of Hexagonal-Phase $NaYF_4$:Yb,Er and $NaYF_4$:Yb,Tm Nanocrystals with Efficient Upconversion Fluorescence. *Adv. Funct. Mater.* **2006**, *16*, 2324−2329.
(67) Liu, Y. S.; Tu, D. D.; Zhu, H. M.; Chen, X. Y. Lanthanide-Doped Luminescent Nanoprobes: Controlled Synthesis, Optical Spectroscopy, and Bioapplications. *Chem. Soc. Rev.* **2013**, *42*, 6924−6958.
(68) Li, Z. Q.; Zhang, Y.; Jiang, S. Multicolor Core/Shell-Structured Upconversion Fluorescent Nanoparticles. *Adv. Mater.* **2008**, *20*, 4765−4969.
(69) Zhang, F.; Wan, Y.; Yu, T.; Zhang, F.; Shi, Y.; Xie, S.; Li, Y.; Xu, L.; Tu, B.; Zhao, D. Uniform Nanostructured Arrays of Sodium Rare-Earth Fluorides for Highly Efficient Multicolor Upconversion Luminescence. *Angew. Chem., Int. Ed.* **2007**, *46*, 7976−7979.
(70) Zhou, H. P.; Xu, C. H.; Sun, W.; Yan, C. H. Clean and Flexible Modification Strategy for Carboxyl/Aldenhyde-Functionalized Upcon-

version Nanoparticles and Their Optical Applications. *Adv. Funct. Mater.* **2009**, *19*, 3892−3900.
(71) Zhang, S. Z.; Sun, L. D.; Tian, H.; Liu, Y.; Wang, J. F.; Yan, C. H. Reversible Luminescence Switching of $NaYF_4$:Yb,Er Nanoparticles with Controlled Assembly of Gold Nanoparticles. *Chem. Commun.* **2009**, 2547−2549.
(72) Ghosh, S. K.; Pal, T. Interparticle Coupling Effect on the Surface Plasmon Resonance of Gold Nanoparticles: From Theory to Applications. *Chem. Rev.* **2007**, *107*, 4797−4862.
(73) Zhang, H.; Li, Y. J.; Ivanov, I. A.; Qu, Y. Q.; Huang, Y.; Duan, X. F. Plasmonic Modulation of the Upconversion Fluorescence in $NaYF_4$:Yb/Tm Hexaplate Nanocrystals Using Gold Nanoparticles or Nanoshells. *Angew. Chem., Int. Ed.* **2010**, *49*, 2865−2868.
(74) Yague, C.; Arruebo, M.; Santamaria, J. NIR-Enhanced Drug Release from Porous Au/SiO_2 Nanoparticles. *Chem. Commun.* **2010**, *46*, 7513−7515.
(75) Zhou, Y.-M.; Wang, H.-B.; Gong, M.; Sun, Z.-Y.; Cheng, K.; Kong, X.-K.; Guo, Z.; Chen, Q.-W. Yolk-Type Au@Fe_3O_4@C Nanospheres for Drug Delivery, MRI and Two-Photon Fluorescence Imaging. *Dalton Trans.* **2013**, *42*, 9906−9913.